Iğdır Üniversitesi Fen Bilimleri Enstitüsü Dergisi, 16(3), 1070-1080, 2026
Journal of the Institute of Science and Technology, 16(3), 1070-1080, 2026

ISSN: 2146-0574, eISSN: 2536-4618

Physics **DOI: 10.21597/jist. 1837264**

Research Article

Received: 06.12.2025 **Accepted: 09.02.2026**

To Cite*:* Bilican, F. (2026). Strain Engineering of Two-Dimensional Penta-Octa $B_4C_2N_3$: Electronic Structure and Optical Response. *Journal of the Institute of Science and Technology*, 16(3), 1070-1080.

Strain Engineering of Two-Dimensional Penta-Octa $B_4C_2N_3$: Electronic Structure and Optical Response

Fuat BİLİCAN[1*]

Highlights:

- Penta–octa $B_4C_2N_3$ monolayer has an indirect band gap of 0.279 eV and a high work function of 5.272 eV
- Biaxial strain induces metal–semiconductor and indirect–direct band-gap transitions
- Optical absorption shows strong sensitivity

Keywords:

- 2D
- Penta-Octa
- $B_4C_2N_3$
- DFT
- Strain Engineering

ABSTRACT:

Two-dimensional (2D) boron–carbon–nitrogen (BCN) systems have recently attracted significant interest owing to their structural stability, electronic diversity, and tunable optical behavior. In this work, the structural, electronic, and optical properties of the 2D penta–octa $B_4C_2N_3$ monolayer are systematically investigated using first-principles calculations. The optimized structure exhibits moderate buckling, multiple distinct bond environments, and energetically favorable cohesive and formation energies. The monolayer is identified as a non-magnetic indirect semiconductor with a band gap of 0.279 eV, where the density of states is dominated by N–p and C–p orbitals. Thermal stability is confirmed by ab initio molecular dynamics simulations at 600 K, and a relatively high work function of 5.272 eV suggests strong surface stability and favorable compatibility with electronic interfaces. Biaxial strain is shown to be highly effective in tuning the electronic structure. Compressive strain (-4% to -2%) induces a semiconductor-to-metal transition, while moderate tensile strain (+1% to +3%) results in an indirect to direct band gap conversion. The band gap can be continuously tuned from 0.11 eV to 0.583 eV under tensile loading. Optical absorption calculations reveal strong light–matter interaction with absorption coefficients reaching 10^4–10^5 cm^{-1}. These results demonstrate that 2D penta–octa $B_4C_2N_3$ is a structurally robust, electronically adaptive, and optically responsive monolayer with strong potential for next-generation strain-engineered optoelectronic and photonic devices.

[1] Fuat BİLİCAN (Orcid ID: 0000-0003-1153-8263), Faculty of Science, Department of Physics , Türkiye

***Corresponding Author:** Fuat BİLİCAN, e-mail: fbilican@pau.edu.tr

INTRODUCTION

Two-dimensional (2D) materials have attracted great attention due to their mechanical flexibility, tunable electronic structures, and promising applicability in next generation nanoelectronics and optoelectronic devices (Lv et al., 2018; Vincent et al., 2021; Ling et al., 2021; Bilican et al., 2025; Bilican et al., 2026). Following the discovery of graphene, interest in new 2D materials composed of light elements such as B, C, and N has grown rapidly, as these elements enable diverse bonding configurations and highly adjustable electronic properties (Novoselov et al., 2004; Zhang et al., 2015; Weng et al., 2018; De Oliveira et al. 2024). In particular, boron–carbon–nitrogen (B–C–N) based 2D materials have emerged as promising candidates for a wide range of advanced technological applications, including energy storage, semiconductor technologies, photo-catalysis, and electro-optical devices (Azevedo & De Paiva 2006; Beniwal et al., 2017; Angizi et al. 2020; Bafekry et al., 2021; Thomas et al. 2024; Wang et al., 2024).

Among the emerging 2D allotropes, 2D penta–octa structures represent an intriguing class in which the coexistence of pentagonal and octagonal rings leads to pronounced anisotropy, high mechanical robustness, and semiconducting electronic characteristics (Laranjeira et al., 2024; Chen et al., 2025). Despite these appealing attributes, the fundamental physical properties of 2D penta–octa BCN monolayers remain largely unexplored. In this context, the 2D penta–octa $B_4C_2N_3$ monolayer, which combines the complementary chemical characteristics of boron, carbon, and nitrogen, emerges as a structurally robust and chemically well-ordered 2D material (Chen et al., 2025). Owing to its distinct bonding environment and low atomic mass, this monolayer is expected to exhibit high mechanical flexibility, making its electronic and optical characteristics particularly sensitive to externally applied strain. Strain engineering, a powerful strategy widely used to tune band gaps and optical absorption spectra in 2D semiconductors, therefore provides an ideal route to modulate the intrinsic properties of $B_4C_2N_3$ without introducing defects or chemical dopants.

Although strain-induced electronic transitions have been widely reported for graphene derivatives, graphyne, T-graphene, h-BN, BP, and various MXene and TMDC monolayers, the strain-dependent behavior of the 2D penta–octa $B_4C_2N_3$ structure has not yet been systematically examined (Vaidyanathan et al., 2025; Majidi, 2017; Thomas et al., 2020; Bilican et al., 2023; Zollner et al., 2019). In particular, the effects of biaxial strain on its optical absorption characteristics, as well as the possibility of a strain-induced indirect to direct band gap transition, remain unexplored in the existing literature.

In this study, first-principles density functional theory (DFT) calculations are employed to investigate the structural stability, strain-induced electronic properties, and optical response of the 2D penta–octa $B_4C_2N_3$ monolayer. The effects of biaxial strain on the band structure, density of states, and optical absorption spectrum are systematically examined to provide deeper insight into the tunability of this promising 2D system.

MATERIALS AND METHODS

All total energy calculations were performed within the framework of density functional theory (DFT) using the Vienna ab initio simulation package (VASP) (Kresse & Hafner, 1993; Kresse & Hafner, 1994; Kresse & Joubert, 1999), which employs the projector augmented wave (PAW) method (Blöchl, 1994) to describe the interaction between valence and core electrons. The exchange–correlation interactions were treated using the generalized gradient approximation (GGA) within the Perdew–Burke–Ernzerhof (PBE) functional (Perdew et al., 1992). Van der Waals (vdW) interactions were included through Grimme's DFT-D2 correction (Grimme, 2006). A kinetic energy cutoff of 550

eV was applied for the plane-wave basis set to ensure the convergence of total energy. Brillouin zone sampling was carried out using a 6×6×1 Monkhorst–Pack k -point mesh (Monkhorst & Pack, 1976). The Gaussian smearing width of 0.01 eV was used for reciprocal-space integration. Structural relaxations to minimize total energy and atomic forces were performed using the conjugate gradient (CG) method (Hestenes & Stiefel, 1952). Convergence criteria were set such that the total energy change between successive steps was below 10^{-5} eV, and the Hellmann–Feynman forces on each atom were less than 10^{-3} eV/A. The vacuum spacing of approximately 24 Å was introduced along the out-of-plane direction to avoid spurious interactions between periodic images. To evaluate the thermal stability of the structures, finite-temperature ab initio molecular dynamics (AIMD) simulations were carried out in the canonical (NVT) ensemble. Simulations were performed at 600 K for 2D penta–octa $B_4C_2N_3$ monolayer. The monolayer was equilibrated for 5 ps using a time step of 1 fs. Temperature control was maintained using the Nosé–Hoover thermostat (Braga & Travis, 2005). The cohesive energy E_{coh} and formation energy E_{for} of 2D penta–octa $B_4C_2N_3$ monolayer was calculated using

$$E_{\text{coh}} = \frac{E_{\text{B}_8\text{C}_4\text{N}_6} - 8E_{\text{B}} - 4E_{\text{C}} - 6E_{\text{N}}}{18}$$

and

$$E_{\text{for}} = E_{\text{B}_8\text{C}_4\text{N}_6} - 8\mu_{\text{B}} - 4\mu_{\text{C}} - 6\mu_{\text{N}}$$

Here, E_B, E_C, and E_N denote the energies of isolated spin-polarized boron, carbon, and nitrogen atoms, respectively, while μ_B, μ_C, and μ_N represent the corresponding chemical potential obtained from the per atom energies of their bulk phases. Electronic band structures were obtained using the sumo-bandplot code (Ganose et al., 2018). Bader charge analysis (Henkelman et al., 2005; Sanville et al., 2007; Tang et al., 2009; Yu & Trinkle, 2011) was performed to quantify charge transfer to quantify charge transfer among B, C, and N atoms in the monolayer. Structural models and visualization of charge distributions were produced using the VESTA software package (Momma & Izumi, 2011).

RESULTS AND DISCUSSION

The optimized atomic configuration of the 2D penta–octa $B_4C_2N_3$ monolayer is illustrated in Figure 1(a). The system adopts a tetragonal geometry with lattice constants of a = b = 6.73 Å (Table 1). The structure shows a mild out-of-plane buckling with a height difference of Δz = 1.31 Å. This value is slightly larger than the 1.23 Å buckling reported for the POG monolayer (Gao & Ren, 2020) and significantly smaller than the 2.07 Å distortion observed in POG-Si_5C_4 (Laranjeira et al. 2024), positioning $B_4C_2N_3$ between these two systems in terms of geometric corrugation. Five distinct bond lengths are identified within the relaxed structure, measured as d_1 = 1.41 Å, d_2 = 1.50 Å, d_3 = 1.60 Å, d_4 = 1.54 Å, and d_5 = 1.50 Å. The monolayer belongs to the non-centrosymmetric space group P4mm (No. 99). The cohesive and formation energies were found to be E_{coh} = −6.550 eV/atom and E_{for} = −0.347 eV, respectively, indicating the energetic stability of the structure. Although phonon dispersion calculations were not repeated in this work, previous literature reports confirm the absence of imaginary phonon modes, demonstrating dynamical stability (Chen et al. 2025). Bader charge analysis indicates that boron atoms act as electron donors, transferring their valence electrons to the more electronegative carbon and nitrogen atoms. In the $B_4C_2N_3$ monolayer, the eight boron atoms contribute a total of 24 valence electrons, which are distributed to the four carbon and six nitrogen atoms. As a result, each carbon atom gains approximately 2.0 e^-, while each nitrogen atom acquires an average of about 2.6 e^-. This charge distribution reflects the strong polarity of the B–C and B–N bonds and highlights the dominant contribution of C- and N orbitals states to the electronic structure near the Fermi level.

Table 1. Calculated structural, electronic and magnetic properties of the 2D penta–octa $B_4C_2N_3$ monolayer, including lattice constant (a = b), cohesive energy (E_{coh}), formation energy (E_{for}), electronic band gap (E_g), work function (Φ), magnetic moment (μ), out-of-plane buckling height (Δz), and the five distinct bond lengths d_x. These parameters confirm the energetic, and electronic stability of the monolayer.

Struc.	a/b	E_{coh} (eV)	E_{for} (eV)	E_g (eV)	Φ (eV)	μ(μ_B)	Δz (Å)	d_x (Å)
$B_4C_2N_3$	6.735	-6.550	-0.347	0.279	5.272	NM	1.31	d_1 = 1.41 d_2 = 1.50 d_3 = 1.60 d_4 = 1.54 d_5 = 1.50

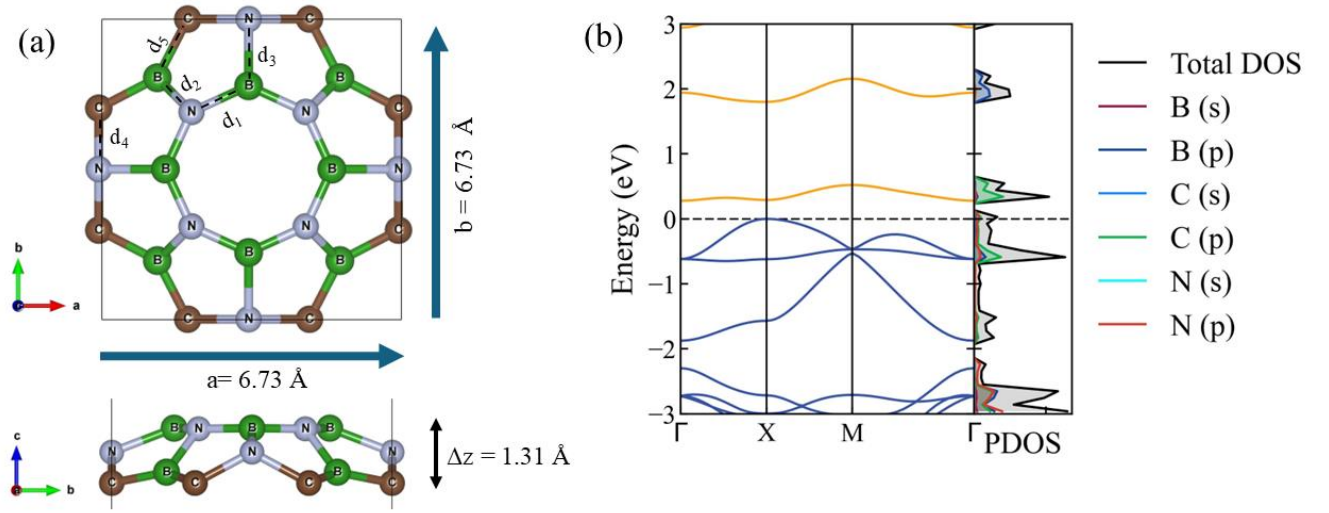

Figure 1. (a) Optimized atomic structure of the 2D penta–octa $B_4C_2N_3$ monolayer, showing the pentagonal–octagonal ring arrangement, lattice parameters, and distinct bond lengths (d_1 –d_5). (b) Electronic band structure and projected density of states (PDOS) at the equilibrium configuration, demonstrating that the monolayer is a non-magnetic indirect semiconductor with a band gap of 0.279 eV

The electronic band structure and projected density of states (PDOS), shown in Figure 1(b), reveal that $B_4C_2N_3$ monolayer is a non-magnetic indirect semiconductor with a band gap of 0.279 eV. The VBM and CBM are located at the X and Γ points, respectively, confirming the indirect band-gap nature of the single-layer structure. The PDOS analysis further shows that the VBM is mainly composed of N–p and C–p orbitals, suggesting strong hybridization between these atoms that stabilizes the top of the valence band. In contrast, the CBM is dominated by C–p states with smaller contributions from B–p orbitals. This indicates that conduction processes are largely governed by the electronic environment around carbon atoms. The asymmetry between the valence and conduction band compositions implies different effective masses for electrons and holes, which may influence carrier mobility and transport anisotropy in this monolayer.

Finite-temperature ab initio molecular dynamics (AIMD) simulations were performed at 600 K for 5 ps to evaluate the thermal stability of the monolayer. As shown in Figure 2(a), the total energy fluctuates within a narrow range around its equilibrium value, indicating that the system maintains dynamical equilibrium throughout the simulation.

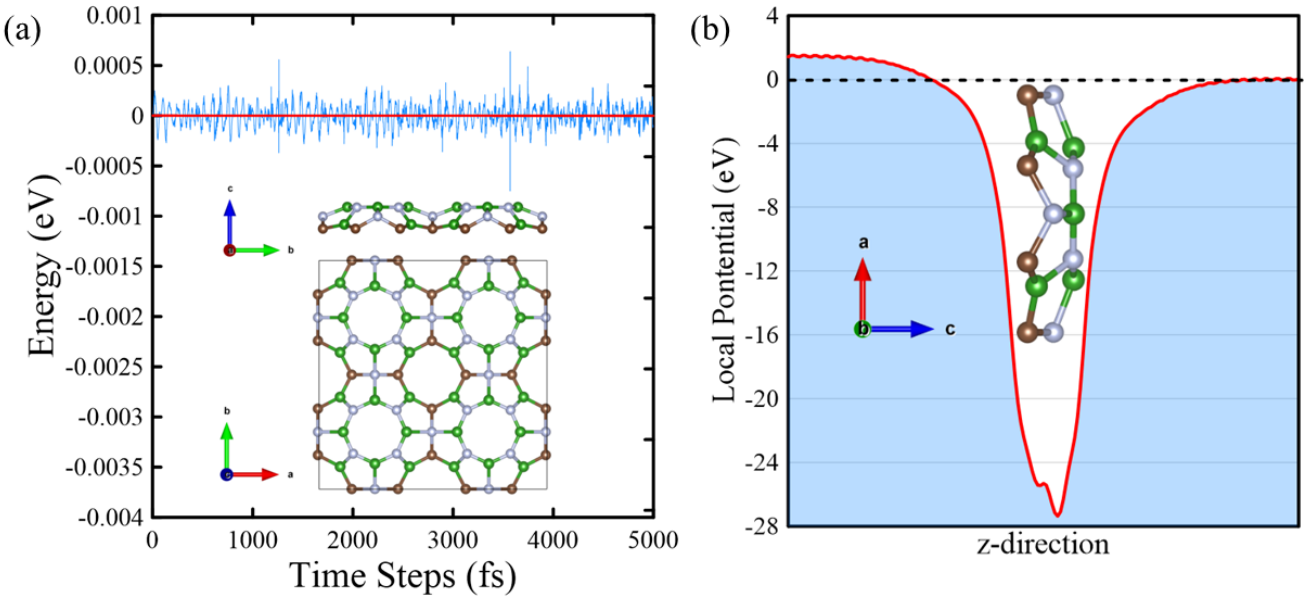

Figure 2. (a) Ab initio molecular dynamics (AIMD) simulation of the 2D penta–octa $B_4C_2N_3$ monolayer at 600 K for 5 ps. The total energy fluctuation indicates thermal stability, while the top and side views confirm that no structural distortion or bond breaking occurs during the simulation. (b) Planar-averaged electrostatic potential along the out-of-plane direction used to determine the work function ($\Phi = E_{vac} - E_F$). The extracted work function value of 5.272 eV reflects strong surface stability of the monolayer

No signs of structural degradation, bond breaking, or topological reconstruction were detected in either the top or side views of the atomic trajectory snapshots. The preservation of all B–C, C–N, and B–N bonds during the simulation confirms that the penta–octa framework is resilient against thermal perturbations. The small amplitude of the energy oscillations further suggests that thermal vibrations are effectively accommodated within the lattice without inducing significant anharmonic distortions. This behavior reflects the strong chemical bonding and mechanical rigidity inherent to the BCN penta–octa configuration. The ability of the monolayer to retain its structural integrity at 600 K (a temperature considerably higher than ambient conditions) demonstrates its robustness and suitability for practical applications in nanoelectronics and optoelectronic devices, where thermal stability is a critical requirement.

The planar-averaged electrostatic potential along the z -direction was used to evaluate the work function, defined as $\Phi = E_{vac} - E_F$. In Figure 2 (b), the vacuum level can be clearly separated from the internal capacity of the sheet; this ensures reliable operation of the work function. The calculated value of $\Phi = 5.272$ eV is relatively high compared to many 2D materials, which indicates that electrons are strongly bound to the surface and require significant energy to escape into the vacuum (Erdem et al. 2024; Niu wt al., 2025; Liu et al., 2025). Moreover, materials with high work functions are frequently employed as hole-injection or electron-blocking layers in optoelectronic architecture such as photo detectors, LEDs, and solar cells (Opitz et al. 2012; Choi et al. 2014; Huang et al. 2020).

To explore the mechanical tunability of the electronic structure, biaxial strain was applied from −4% to +10%, and the resulting band dispersions are presented in Figure 3. Under compressive strains of −4%, −3%, and −2%, the band gap closes completely, leading to a metallic phase. This metallicity is caused by the upward shift of the valence band maximum and the downward shift of the conduction band minimum, which results in band overlapping near the Fermi level. At −1% strain, the overlap disappears, and a metal–semiconductor transition occurs, reopening indirect band gap. Notably, when small tensile strains of +1%, +2%, and +3% are applied, the monolayer undergoes an indirect to direct band gap transition.

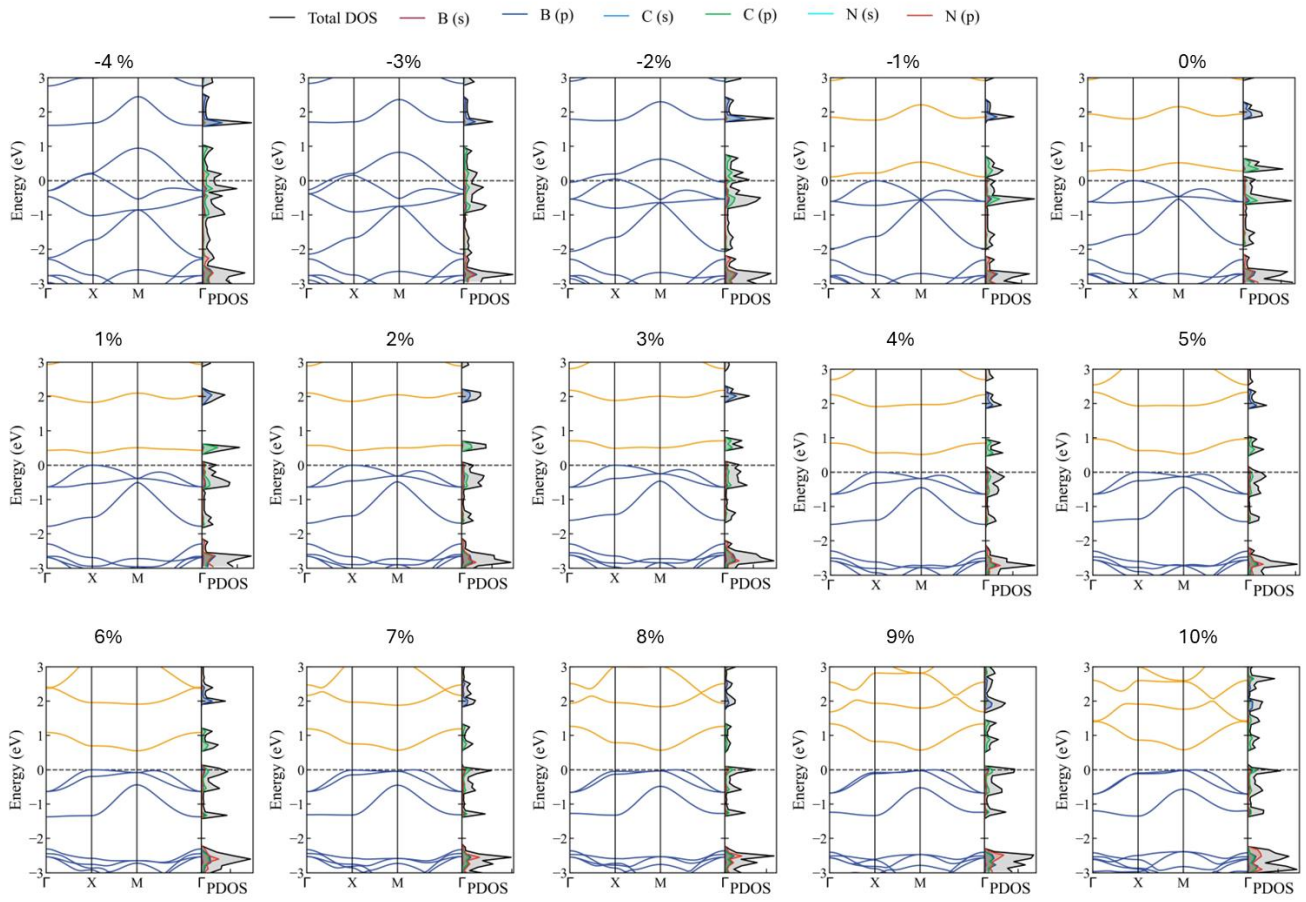

Figure 3. Electronic band structures and projected density of states (PDOS) of the 2D penta–octa $B_4C_2N_3$ monolayer under biaxial strain from −4% to +10%. Compressive strains of −4% to −2% induce metallic behavior, while the system remains semiconducting with an indirect band gap at −1% strain and in the equilibrium state. An indirect-to-direct band-gap transition occurs at +1%, +2% and +3% tensile strain, followed by a reversion to an indirect band gap for strains between +4% and +10%. The PDOS reveals the strain-dependent contribution of B-, C-, and N-p orbitals

These moderate tensile strains modify the dispersion and relative alignment of the band edges such that both the VBM and CBM move to the same high-symmetry point. This strain-induced direct band gap regime enables momentum-conserving optical transitions, which is advantageous for optoelectronic performance. For larger tensile strains (from +4% up to +10%), the system remains semiconducting but reverts to an indirect band gap. This indicates that the direct-gap configuration is stabilized only within a relatively narrow strain window, while broader tensile deformation shifts the band edges back into an indirect arrangement. Such sensitivity of the band topology to moderate lattice deformation highlights the potential of $B_4C_2N_3$ monolayer for strain-controlled electronic and optical switching applications. The band gap values vary from approximately 0.11 eV at tensile strain to 0.583 eV at +10% strain, as summarized in Figure 4. This wide tunability demonstrates that the electronic structure of $B_4C_2N_3$ is highly sensitive to mechanical deformation.

The optical absorption spectra under biaxial strain are presented in Figure 5. The absorption coefficient reaches values on the order of 10^4 –10^5 cm^{-1} across the studied energy range, confirming that $B_4C_2N_3$ monolayer exhibits strong light–matter interaction like other optically active 2D semiconductors. The optical band gap, indicated by the vertical dotted lines in the figure, varies between 0.12 eV and 0.67 eV depending on the applied strain. This pronounced tunability is consistent with the electronic band gap evolution discussed in Figure 4, reflecting the strain-induced modifications in density of states and transition probabilities.

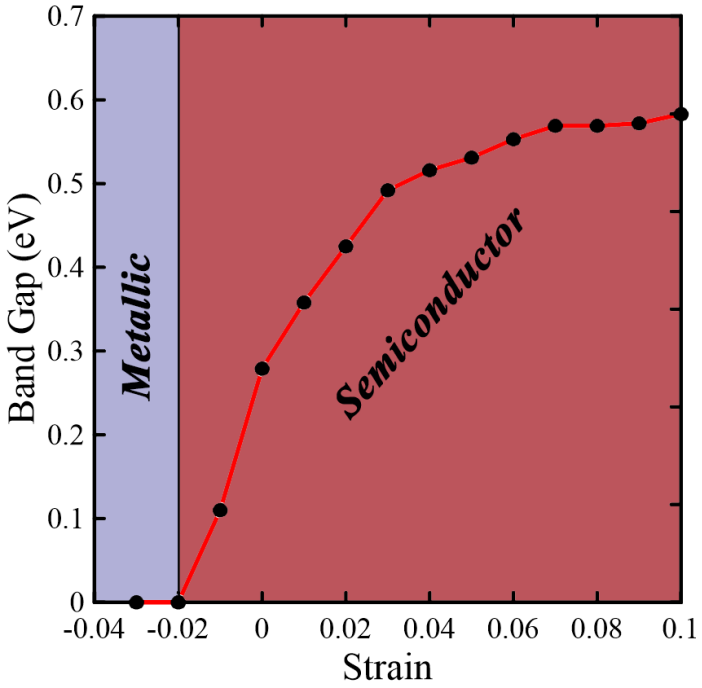

Figure 4. Strain-dependent band gap variation of the 2D penta–octa $B_4C_2N_3$ monolayer under biaxial deformation ranging from −4% to +10%. The band gap closes completely for compressive strains between −4% and −2%, indicating a metallic phase. For strains from −1% to +10%, the band gap reopens and the monolayer preserves its semiconducting character, exhibiting tunable band gaps between 0.11 eV and 0.583 eV. This strong strain-induced modulation highlights the mechanical controllability of the electronic properties in $B_4C_2N_3$ monolayer

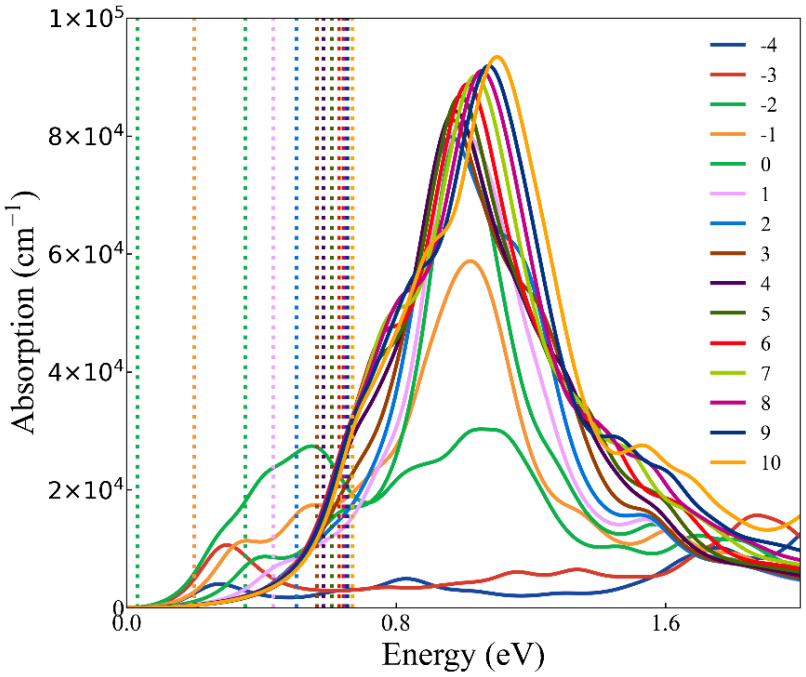

Figure 5. Strain-dependent optical absorption spectra of the 2D penta–octa $B_4C_2N_3$ monolayer under biaxial strain values ranging from −4% to +10%. The absorption onset (optical band gap) varies between 0.12 eV and 0.67 eV depending on the applied strain. For compressive strains of −4% to −2%, the absorption spectra display broad low-energy features, consistent with the metallic nature of the monolayer in this regime. For strains between −1% and +10%, well-defined absorption edges and characteristic peaks emerge, reflecting the semiconducting behavior of the structure. These results demonstrate strong strain-induced tunability of the optical response, highlighting the potential of the monolayer for flexible optoelectronic applications

Tensile strain enlarges the band gap, which increases the minimum photon energy required for electronic transitions. As a result, the absorption onset shifts toward higher energies, producing a characteristic blue-shift in the optical spectrum. Conversely, compressive strain, particularly in the metallic regime (–4% to –2%), introduces low-energy absorption features and suppresses the formation of a sharp absorption edge, which is characteristic of metals with free-carrier contributions. For semiconducting strains (–1% to +10%), the spectra recover well-defined absorption edges and distinct peaks, indicating the re-establishment of direct electronic transitions within the monolayer. These observations collectively demonstrate that the optical response of $B_4C_2N_3$ is highly sensitive to mechanical deformation. The ability to reversibly modulate both the position and intensity of absorption features through biaxial strain highlights the potential of this material for tunable photonic and optoelectronic applications, including infrared detectors, strain-controlled modulators, and flexible optical devices.

These results demonstrate that $B_4C_2N_3$ monolayer exhibits strong optical tunability and holds significant potential for application in strain-engineered optoelectronic and photonic devices.

CONCLUSION

In this study, the structural, electronic, and optical properties of the 2D penta–octa $B_4C_2N_3$ monolayer were systematically investigated through first principles calculations. The optimized geometry exhibits moderate buckling, multiple distinct bond environments, and energetically favorable cohesive and formation energies, confirming the intrinsic stability of the lattice. The monolayer is identified as a non-magnetic indirect semiconductor with a band gap of 0.279 eV, where the band edges are dominated by N–p and C–p orbitals. Thermal robustness is further validated by AIMD simulations at 600 K, which reveal preserved structural integrity without bond breaking or reconstruction. The material also possesses a relatively high work function of 5.272 eV, suggesting strong surface stability and promising compatibility with interface-engineered electronic and optoelectronic devices. Biaxial strain was shown to be an effective route for tuning the electronic structure of $B_4C_2N_3$. Compressive strain induces a semiconductor to metal transition, while moderate tensile strain (1% – 3%) enables an indirect to direct band-gap transformation. At larger tensile strains, the system remains semiconducting but recovers an indirect band gap. Overall, the band gap can be tuned over a wide range (0.11 – 0.583 eV), demonstrating strong mechanical sensitivity and potential for strain-controlled electronic switching. Consistent with the electronic trends, the optical absorption response also exhibits remarkable tunability under strain. Tensile loading produces a pronounced blue-shift in the absorption onset, whereas compressive strain broadens the low-energy spectrum due to metallic free-carrier effects. Well-defined absorption edges and strain-dependent interband-transition peaks re-emerge in the semiconducting regime. The strong light–matter interaction, combined with reversible optical modulation, highlights the capability of $B_4C_2N_3$ as a versatile material platform for mechanically tunable photonic and optoelectronic applications, including infrared detection, flexible optical components, and strain-responsive device architectures. Overall, the results demonstrate that 2D penta–octa $B_4C_2N_3$ is a structurally stable, electronically adaptive, and optically responsive 2D material with strong potential for next-generation strain-engineered technologies.

ACKNOWLEDGEMENTS

The calculations were performed at the National Center for High-Performance Computing of Turkey (UHEM) under Grant No. 5024802025. This study was supported by the Pamukkale

University Scientific Research Projects Unit (Project Number: 2025BSP009). I also thank the PAU Materials Physics Simulation Laboratory for their infrastructure and technical support.

REFERENCES

Angizi, S., Akbar, M. A., Darestani-Farahani, M., & Kruse, P. (2020). Review—Two-Dimensional Boron Carbon Nitride: A Comprehensive Review. ECS Journal of Solid State Science and Technology, 9(8), 083004. https://doi.org/10.1149/2162-8777/abb8ef

Azevedo, S., & De Paiva, R. (2006). Structural stability and electronic properties of carbon-boron nitride compounds. Europhysics Letters (EPL), 75(1), 126–132. https://doi.org/10.1209/epl/i2006-10066-0

Bafekry, A., Naseri, M., Fadlallah, M. M., Sarsari, I. A., Faraji, M., Khatibani, A. B., Ghergherehchi, M., & Gogova, D. (2021). A novel two-dimensional boron–carbon–nitride (BCN) monolayer: A first-principles insight. Journal of Applied Physics, 130(11). https://doi.org/10.1063/5.0062323

Beniwal, S., Hooper, J., Miller, D. P., Costa, P. S., Chen, G., Liu, S.-Y., Dowben, P. A., Sykes, E. C. H., Zurek, E., & Enders, A. (2017). Graphene-like Boron–Carbon–Nitrogen monolayers. ACS Nano, 11(3), 2486–2493. https://doi.org/10.1021/acsnano.6b08136

Bilican, F., Kart, S. O., Vatansever, E., Ersan, F., & Vatansever, Z. D. (2023). Strain effects on the electronic and magnetic properties of Cr_2TaC_2 and $Cr_2TaC_2O_2$ monolayers. Applied Physics Letters, 122(15). https://doi.org/10.1063/5.0142420

Bilican, F. (2025). Tailoring electronic and magnetic properties of dodecagonal graphene via atom substitution: A DFT study. Micro and Nanostructures, 208, 208335. https://doi.org/10.1016/j.micrna.2025.208335

Bilican, F., Ersan, F., Vatansever, Z. D., Kart, S. O., & Vatansever, E. (2026). Electronic and magnetic properties of FeX_4 (X = N, P) monolayer and bilayer structures under strain. *Physical Review Applied*, *25*(1). https://doi.org/10.1103/btqb-5vh2

Blöchl, P. E. (1994). Projector augmented-wave method. Physical Review. B, Condensed Matter, 50(24), 17953–17979. https://doi.org/10.1103/physrevb.50.17953

Braga, C., & Travis, K. P. (2005). A configurational temperature Nos´e-Hoover thermostat. The Journal of Chemical Physics, 123(13), 134101. https://doi.org/10.1063/1.2013227

Chen, X., Wang, J., Martins, N. F., Sambrano, J. R., & Laranjeira, J. a. S. (2025). Penta-Octa $B_4C_2N_3$: a new 2D material for High-Performance Energy applications. Langmuir, 41(8), 5477–5487. https://doi.org/10.1021/acs.langmuir.4c05139

Choi, H., Kim, H., Ko, S., Kim, J. Y., & Heeger, A. J. (2014). An organic surface modifier to produce a high work function transparent electrode for high performance polymer solar cells. Advanced Materials, 27(5), 892–896. https://doi.org/10.1002/adma.201404172

De Oliveira, R. B., Santos, O. F. P. D., Azevedo, S., & Machado, L. D. (2024). On the role of the interface in the mechanical and electronic properties of BCN monolayers. Diamond and Related Materials, 145, 111070. https://doi.org/10.1016/j.diamond.2024.111070

Erdem, I., F., Kart, H. H., Kart, S. O., & Ersan, F. (2024). Point defects in Dirac semimetal BeN_4 monolayer and their interaction with gas molecules. Vacuum, 222, 113095. https://doi.org/10.1016/j.vacuum.2024.113095

Ganose, A. M., Jackson, A. J., & Scanlon, D. O. (2018). sumo: Command-line tools for plotting and analysis of periodic ab initio calculations. The Journal of Open Source Software, 3(28), 717. https://doi.org/10.21105/joss.00717

Gao, H., & Ren, W. (2020). Emergence of Type-I and Type-II Dirac line nodes in penta-octa-graphene. Carbon, 158, 210–215. https://doi.org/10.1016/j.carbon.2019.11.083

Grimme, S. (2006). Semiempirical GGA-type density functional constructed with a long-range dispersion correction. Journal of Computational Chemistry, 27(15), 1787–1799. https://doi.org/10.1002/jcc.20495

Henkelman, G., Arnaldsson, A., & J´onsson, H. (2005). A fast and robust algorithm for Bader decomposition of charge density. Computational Materials Science, 36(3), 354–360. https://doi.org/10.1016/j.commatsci.2005.04.010

Hestenes, & Stiefel, E. (1952). Methods of conjugate gradients for solving linear systems. Journal of Research of the National Bureau of Standards, 49(6), 409. https://doi.org/10.6028/jres.049.044

Huang, Z., Zhong, Z., Wang, H., Lu, S., Wang, J., Liu, G., Wei, T., Yan, J., Min, J.-H., Jeong, W. L., Lee, D.-S., Cai, X., Xu, F., Chen, X., Cai, D., Wang, J., Kang, J., Huang, Z., Zhong, Z., . . . Kang, J. (2020). Enhanced Emission of Deep Ultraviolet Light-Emitting Diodes through Using Work Function Tunable Cu Nanowires as the Top Transparent Electrode. The Journal of Physical Chemistry Letters, 11(7), 2559–2569. https://doi.org/10.1021/acs.jpclett.0c00653

Kresse, G., & Hafner, J. (1993). Ab initiomolecular dynamics for liquid metals. Physical Review. B, Condensed Matter, 47(1), 558–561. https://doi.org/10.1103/physrevb.47.558

Kresse, G., & Hafner, J. (1994). Ab initiomolecular-dynamics simulation of the liquid-metal–amorphous-semiconductor transition in germanium. Physical Review. B, Condensed Matter, 49(20), 14251–14269. https://doi.org/10.1103/physrevb.49.14251

Kresse, G., & Joubert, D. (1999). From ultrasoft pseudopotentials to the projector augmented-wave method. Physical Review. B, Condensed Matter, 59(3), 1758–1775. https://doi.org/10.1103/physrevb.59.1758

Laranjeira, J. a. S., Martins, N. F., Denis, P. A., & Sambrano, J. R. (2024). A novel and promising Penta-Octa-Based silicon carbide semiconductor. FlatChem, 46, 100691. https://doi.org/10.1016/j.flatc.2024.100691

Lv, P., Tang, G., Yang, C., Deng, J., Liu, Y., Wang, X., Wang, X., & Hong, J. (2018). Half metallicity in two-dimensional Co_2Se_3 monolayer with superior mechanical flexibility. 2D Materials, 5(4), 045026. https://doi.org/10.1088/2053-1583/aadb5a

Ling, Z. P. (2021). Two-Dimensional (2D) materials for Next-Generation nanoelectronics and Optoelectronics: Advances and Trends. In Advances in material research and technology (pp. 65–96). https://doi.org/10.1007/978-3-030-57737-7 3

Liu, W., Wu, Y., Bao, X., Sun, L., Xie, Y., & Chen, Y. (2025). High-Performance Infrared Self-Powered Photodetector Based on 2D Van der Waals Heterostructures. Advanced Functional Materials, 35(26). https://doi.org/10.1002/adfm.202421525

Majidi, R. (2017). Density functional theory study on structural and mechanical properties of graphene, T-graphene, and R-graphyne. Theoretical Chemistry Accounts, 136(9). https://doi.org/10.1007/s00214-017-2148-1

Momma, K., & Izumi, F. (2011). VESTA 3 for three-dimensional visualization of crystal, volumetric and morphology data. Journal of Applied Crystallography, 44(6), 1272–1276. https://doi.org/10.1107/s0021889811038970

Monkhorst, H. J., & Pack, J. D. (1976). Special points for Brillouin-zone integrations. Physical Review B, Solid State, 13(12), 5188–5192. https://doi.org/10.1103/physrevb.13.5188

Novoselov, K. S., Geim, A. K., Morozov, S. V., Jiang, D., Zhang, Y., Dubonos, S. V., Grigorieva, I. V., & Firsov, A. A. (2004b). Electric field effect in atomically thin carbon films. Science, 306(5696), 666–669. https://doi.org/10.1126/science.1102896

Niu, X., Niu, Z., Shan, W., Shi, A., Wang, X., & Zhang, X. (2025). 2D electron Gas-Induced the lowered tunneling barrier and Ohmic behavior simultaneously in 2D Metal-Semiconductor contacts. Advanced Functional Materials. https://doi.org/10.1002/adfm.202513567

Opitz, A., Frisch, J., Schlesinger, R., Wilke, A., & Koch, N. (2012). Energy level alignment at interfaces in organic photovoltaic devices. Journal of Electron Spectroscopy and Related Phenomena, 190, 12–24. https://doi.org/10.1016/j.elspec.2012.11.008

Perdew, J. P., Chevary, J. A., Vosko, S. H., Jackson, K. A., Pederson, M. R., Singh, D. J., & Fiolhais, C. (1992). Atoms, molecules, solids, and surfaces: Applications of the generalized gradient approximation for exchange and correlation. Physical Review. B, Condensed Matter, 46(11), 6671–6687. https://doi.org/10.1103/physrevb.46.6671

Sanville, E., Kenny, S. D., Smith, R., & Henkelman, G. (2007). Improved grid-based algorithm for Bader charge allocation. Journal of Computational Chemistry, 28(5), 899–908. https://doi.org/10.1002/jcc.20575

Tang, W., Sanville, E., & Henkelman, G. (2009). A grid-based Bader analysis algorithm without lattice bias. Journal of Physics Condensed Matter, 21(8), 084204. https://doi.org/10.1088/0953-8984/21/8/084204

Thomas, S. A., Cherusseri, J., Pallavolu, M. R., Rajendran, D. N., & Kumar, D. (2024). Boron Carbon Nitride (BCN): an emerging Two-Dimensional material for rechargeable batteries. Energy & Fuels, 38(15), 13704–13721. https://doi.org/10.1021/acs.energyfuels.4c02056

Thomas, S., Manju, Ajith, K. M., Lee, S. U., & Zaeem, M. A. (2020). Strain-induced work function in h-BN and BCN monolayers. Physica E Low-Dimensional Systems and Nanostructures, 123, 114180. https://doi.org/10.1016/j.physe.2020.114180

Vaidyanathan, A., Wagh, V., & Chakraborty, B. (2025). A strain-engineering approach to enhance hydrogen storage in 2D holey graphyne. International Journal of Hydrogen Energy, 125, 266–276. https://doi.org/10.1016/j.ijhydene.2025.04.010

Vincent, T., Liang, J., Singh, S., Castanon, E. G., Zhang, X., McCreary, A., Jariwala, D., Kazakova, O., & Balushi, Z. Y. A. (2021). Opportunities in electrically tunable 2D materials beyond graphene: Recent progress and future outlook. Applied Physics Reviews, 8(4). https://doi.org/10.1063/5.0051394

Wang, J., & Luo, X. (2024). Theoretical investigation of the BCN monolayer and their derivatives for metal-free CO_2 photocatalysis, capture, and utilization. ACS Omega, 9(3), 3772–3780. https://doi.org/10.1021/acsomega.3c07795

Weng, Q., Li, G., Feng, X., Nielsch, K., Golberg, D., & Schmidt, O. G. (2018). Electronic and Optical Properties of 2D Materials Constructed from Light Atoms. Advanced Materials, 30(46), e1801600. https://doi.org/10.1002/adma.201801600

Yu, M., & Trinkle, D. R. (2011). Accurate and efficient algorithm for Bader charge integration. The Journal of Chemical Physics, 134(6), 064111. https://doi.org/10.1063/1.3553716

Zhang, M., Gao, G., Kutana, A., Wang, Y., Zou, X., Tse, J. S., Yakobson, B. I., Li, H., Liu, H., & Ma, Y. (2015). Two-dimensional boron–nitrogen–carbon monolayers with tunable direct band gaps. Nanoscale, 7(28), 12023–12029. https://doi.org/10.1039/c5nr03344f

Zollner, K., Faria, P. E., Junior, & Fabian, J. (2019). Strain-tunable orbital, spin-orbit, and optical properties of monolayer transition-metal dichalcogenides. Physical Review. B./Physical Review. B, 100(19). https://doi.org/10.1103/physrevb.100.195126